CrystEngComm

Cite this: *CrystEngComm*, 2012, **14**, 8044–8048

www.rsc.org/crystengcomm

PAPER

Mesoporous ZnS hierarchical nanostructures: facile synthesis, growth mechanism and application in gas sensing†

Ruimin Xing,[a] Yan Xue,[b] Xiaoqiang Liu,[a] Baoshun Liu,[c] Baoji Miao,[d] Wenzhe Kang[a] and Shanhu Liu*[a]

Received 9th August 2012, Accepted 31st August 2012
DOI: 10.1039/c2ce26269j

Mesoporous zinc sulfide hierarchical nanostructures were prepared in the presence of polyvinylpyrrolidone aqueous solution *via* a low-cost, hydrothermal route. Field-emission scanning electron microscopy, transmission electron microscopy, X-ray powder diffraction, N_2 adsorption–desorption analysis, and thermal gravimetric analysis were used to characterize the morphology, structure and composition of the products. Results show that the products exhibit a kind of hierarchical structure with mesoporous features which consist of smaller building blocks (*ca.* 30 nm) assembled together. The effects of a series of reaction parameters on the morphology of ZnS nanostructures have been studied systematically. A plausible mechanism based on coordination nucleation and subsequent Ostwald ripening is proposed. By virtue of the interesting porous structure, a chemical sensor was fabricated. The sensor exhibits attractive gasoline sensing behavior with excellent selectivity and fast response.

1 Introduction

The exploration of facile and economic methods for the fabrication of porous materials has accelerated intense and rapid development in the field of material synthesis.[1–5] In particular, mesoporous materials are of scientific and technological importance because they possess high specific surface area, more active sites, and abundant inner spaces, which endow the ability to accomodate various guest molecules within their interior surfaces and the nanometer-sized pore space.[6–8] They offer extensive opportunities in catalysis, sensing, biomedical and optical applications.[9,10] Recently, hierarchical nanostructures with mesoporous features have attracted particular interest in practical applications.[11,12] From the viewpoint of gas sensors, hierarchical nanostructures with mesoporous features are promising candidates because their special structures could greatly facilitate gas diffusion and mass transport in sensor material, thus improving sensor performance.[13,14]

Zinc sulfide (ZnS) is a wide-band gap semiconductor of 3.66 eV for cubic zinc blend phase and of 3.80 eV for hexagonal wurtzite phase. Nanostructured ZnS can offer unique photonic, electronic, and catalytic properties that are of interest for applications as phosphors, bioimaging, sensing, and photocatalysis.[15–19] Besides the sporadic reports on the synthesis of porous ZnS nanostructures in the presence of organic solvent,[20–24] traditional methods usually result in solid nanostructures (such as nanospheres,[25] nanowires,[26] and nanobelts[27]) or hollow nanostructures with fewer active sites[28–30] compared to the porous structures.[31–33] Therefore, the development of cost-effective aqueous solution methods suitable for the large scale synthesis of porous ZnS nanostructures represents a critical challenge to their practical applications.

Herein, we report a low-cost hydrothermal synthetic route to produce monodispersed mesoporous ZnS hierarchical nanostructures (ZnS MHNSs). Microstructural analysis shows that the product consists of primary nanoparticles (*ca.* 30 nm) as building blocks assembled together to form the hierarchical structures with mesoporous features. The effects of reaction duration, temperature, and concentration of reagents on the products have been studied systematically and a plausible mechanism is proposed. As a demonstration of application with ZnS MHNSs, a gasoline sensor with excellent selectivity and fast response was achieved.

2 Experimental section

2.1 Materials

Polyvinylpyrrolidone (PVP, Mw 40 000), poly(diallyldimethylammonium chloride) (PDDA, 20%, Mw 200 000–350 000), and cetyl trimethylammonium bromide (CTAB) were purchased from Sigma-Aldrich Chemical Reagent Co., Ltd. $Zn(Ac)_2{\cdot}2H_2O$, thioacetamide (TAA) and other chemical reagents were obtained from Nanjing Chemical Reagent Co., Ltd. All chemicals were directly used as received without further purification.

[a]*Institute of Molecular and Crystal Engineering, College of Chemistry and Chemical Engineering, Henan University, Kaifeng 475001, P.R. China. E-mail: shanhuliu@henu.edu.cn; Tel: +86-378-3881589*
[b]*Xinxiang University, Xinxiang 453003, P.R. China*
[c]*State Key Laboratory of Silicate Materials for Architectures, Wuhan University of Technology, Wuhan City, Hubei Province 430070, China*
[d]*School of Materials Science and Engineering, Henan University of Technology, Zhengzhou, P.R.China*
† Electronic supplementary information (ESI) available. See DOI: 10.1039/c2ce26269j

2.2 Preparation of ZnS MHNSs

ZnS MHNSs were synthesized *via* a facile hydrothermal procedure. In a typical synthesis, 1.5 g of PVP was added in 10 mL of 50 mmol L^{-1} $ZnAc_2$ aqueous solution and mixed for 6 h with continuous stirring. After that, 10 mL of 50 mmol L^{-1} TAA aqueous solution was added into the mixed solution. The mixture was stirred vigorously to give a homogeneous solution. Then, the solution was transferred into a Teflon-lined stainless steel autoclave (25 mL capacity) for hydrothermal treatment at 180 °C for 12 h. After the autoclave was allowed to cool down to room temperature, the white solid product was collected and washed several times under sonication with water and ethanol, then dried under vacuum at room temperature before characterization and application.

To investigate the influence of experimental conditions (the types of surfactants, concentrations of reagents, temperature, and reaction time) on the morphologies of the ZnS nanostructures, several sets of control experiments were carried out. Each control experiment was performed in the same conditions and using the same procedure as the typical experiment except the change of the parameter mentioned.

2.3 Gas sensor fabrication and response test

The gas-sensing experiments were operated in a measuring system of HWC-30A (Hanwei Electronics Co., Ltd., China). The products were mixed with ethanol and sonicated to form a suspension paste. No conductive binder was added. The paste was coated on ceramic tubes, on which a pair of Au electrodes and two platinum wires were attached for resistance measurements. A Ni–Cr alloy coil was placed through the tube as a heater and different voltages were applied to provide different working temperatures of the sensors. The gas response of the sensor in this paper was defined as $S = R_a/R_g$, where R_a and R_g represent the resistance of a sensor in air and a target reducing gas, respectively. On the other hand, if a target is an oxidizing gas, $S = R_g/R_a$.

2.4 Characterization

Field emission scanning electron microscopy (FE-SEM) images and X-ray energy dispersive spectra (EDX) were obtained using an Hitachi S-4800 field emission electron microscope at an accelerating voltage of 10 kV. Transmission electron microscopy (TEM) images and selected area electron diffraction (SAED) patterns were taken using a JEOL JEM-2100 transmission electron microscope at an accelerating voltage of 200 kV. X-Ray powder diffraction (XRD) measurements were performed on a Japan Shimadzu XRD-6000 diffractometer with Cu Kα radiation ($\lambda = 0.15418$ nm); a scanning rate of 0.05° s^{-1} was applied to record the patterns in the 2θ range of 10–90°. N_2 adsorption–desorption isotherms were obtained at 77 K on ASAP 2020 volumetric adsorption equipment made by Micromeritics Instrument Corporation. The sample was pretreated for 12 h at 373 K under nitrogen before measurements. The specific surface area was calculated by the Brunauer–Emmett–Teller (BET) method. The total pore volume was estimated from single point adsorption at $P/P_0 = 0.99$ and the pore size was derived from the adsorption branch by using the Barrett–Joyner–Halenda (BJH) model. Fourier transform infrared (FT-IR) spectra were recorded on a Nicolet 6700 Fourier transform infrared spectrograph in the range of 4000–500 cm^{-1}. Thermal gravimetric analysis (TGA) was performed on a Pyris 1 DTA instrument.

3 Results and discussion

3.1 Characterization of ZnS MHNSs

The preparation of ZnS MHNSs is quite simple and cost-effective, in that the reactants $ZnAc_2 \cdot 2H_2O$ and TAA only need to react in the presence of PVP aqueous solution under the hydrothermal conditions. By tuning various reaction conditions such as the concentration, the reaction temperature and the time, ZnS MHNSs were successfully synthesized.

The morphology and size distribution of the products were investigated by using SEM. As Fig. 1a presents, the products show an excellent monodispersity and a well-defined spherical shape in large domains. Statistical analyses indicate that the nanospheres have a relatively narrow size distribution, with an average diameter of 200 nm. The high-resolution SEM image in Fig. 1b demonstrates that many primary nanoparticles aggregate to form a spherical three-dimensional, hierarchical nanosphere with a distinct porous structure. In the XRD patterns (Fig. 1c), all diffraction peaks and positions match well with those from the standard JCPDF card (no. 01-0792) for the cubic zinc blend structure with the lattice constants of $a = b = c = 5.40$ Å. Calculations using the Debye–Scherrer formula for the strongest peak (111) show the grain sizes to be about 28 nm. Its EDX spectra in Fig. 1d shows the significant presence of Zn and S, besides the peaks for Cu and C, which arise from the supporting grid of Cu and covering film of C in the sample preparation, respectively. Based on the relative area under the peaks for Zn and S, the atomic ratio of Zn to S is evaluated to be approx. 1 : 1, being in good agreement with the stoichiometric molar ratio of zinc sulfide.

Detailed structural information was obtained by TEM. As a representative TEM image shown in Fig. 2a, the nanospheres consist of primary nanoparticles (*ca.* 30 nm) as building blocks assembled together. Its SAED patterns (Fig. 2b) obtained from

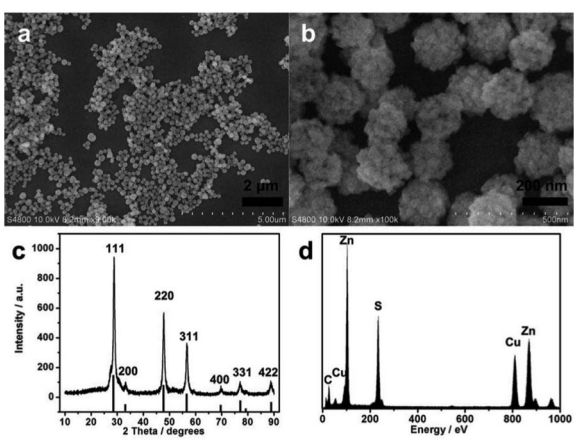

Fig. 1 Low-magnification SEM image (a), high-magnification SEM image (b), XRD patterns (c), and EDX spectra (d) of ZnS MHNSs.

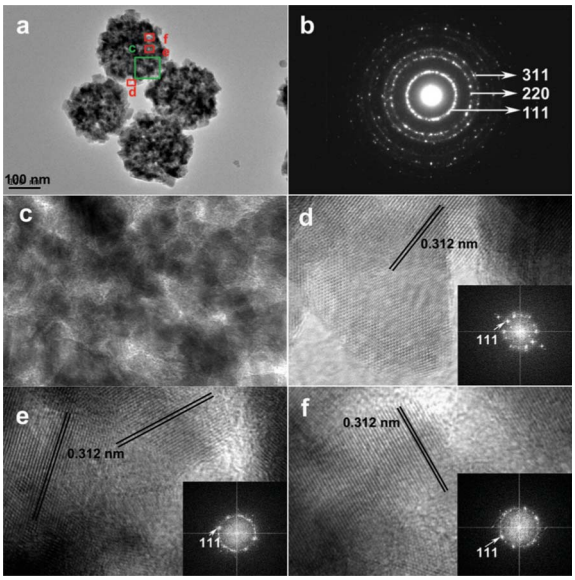

Fig. 2 Low-magnification TEM image (a), SAED patterns (b) and high-magnification TEM images of the framed area marked in a (c–f) of ZnS MHNSs. Insets are their respective FFT patterns.

an isolated nanosphere show the characteristic diffuse electron diffraction rings, indicative of the polycrystalline-like diffraction profiles. More evidence on the crystallinity and the porous structure was obtained from the HRTEM analysis. The distinct contrast within the nanospheres was derived from the difference in electron density, indicating the presence of pores between these interconnected primary nanoparticles and therefore the porous structure of the nanospheres (Fig. 2c). The red marked regions in Fig. 2a were enlarged in Fig. 2d–2f, respectively; and their correlative Fast Fourier Transform (FFT) patterns were extracted as their respective insets to obtain some crystallographic information. These primary nanoparticles display clear lattice fringes with the spacings of 0.312 nm, corresponding to the high crystallinity of (111) planes. All of the FFT patterns show a diffraction pattern corresponding to (111) planes of cubic zinc blend ZnS but with different crystallographic orientations.

N_2 absorption and desorption analysis was used to further examine the porous structure and the data is shown in Fig. 3. The isotherms feature the type IV curves with a hysteresis loop in

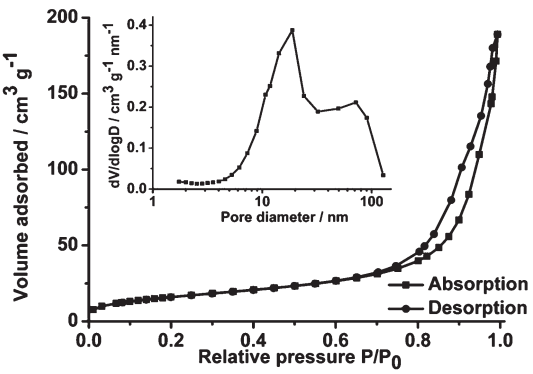

Fig. 3 N_2 adsorption–desorption isotherms and pore size distribution plot (inset) of ZnS MHNSs.

the relatively high pressure range, which is related to the existence of mesopores. The specific surface area and pore volume are determined at about 58 $m^2\ g^{-1}$ and 0.292 $cm^3\ g^{-1}$, respectively. These are not very high because the pores embedded in the nanospheres have a smaller inner surface. The broad pore size distribution of 5–30 nm (inset of Fig. 3) indicates mesoporous features, presumably due to the hierarchically irregular assembly of primary nanoparticles. The BET analysis strongly supports the fact that the nanospheres have a mesoporous structure and more active sites present, which are attractive for sensing and catalysis applications.

3.2 Possible formation mechanism of ZnS MHNSs

To investigate the influence of PVP on the formation of the hierarchical nanostructures with mesoporous features, control A was done to prepare nanostructures in the presence of other surfactants such as PDDA and CTAB instead of PVP. No porous structures were obtained (ESI,† Fig. S1), indicating that PVP is suitable and effective for the formation of ZnS MHNSs in the current hydrothermal method.

The involvement of PVP or its fragments in ZnS MHNSs was studied by FT-IR spectroscopy (ESI,† Fig. S2). The IR peaks of PVP at 3417, 2946, 1658, and 1287 cm^{-1} are assigned to the stretching vibrations of –OH, $–CH_2$, –C=O, and –CN, respectively, as well as the peak of 1438 cm^{-1} from the bending vibration of the –CH group of the pyrrole rings. Comparing with the IR spectra of PVP, ZnS MHNSs show similar absorptions as PVP except the position shifts and the intensity changes to some extent. This evidence not only confirms the existence of PVP or its fragments in ZnS MHNSs, but also indicates that there might be coordination interaction between zinc ions and PVP, which may play a crucial role in regulating the size, shape, and assembly behavior of ZnS MHNSs.

It is of great significance to study the growth mechanism of the porous structure, which would direct the design and fabrication of other similar materials. Generally, the kinetic factors such as the concentration, temperature, and time determine the chemical process.[34–36] Therefore, the concentration-dependent, temperature-dependent, and time-dependent shape evolution of ZnS nanostructures was studied. Fig. S3, ESI,† presents the typical morphology of the products formed with different concentrations of PVP. The product formed in the absence of PVP exhibits irregular shape and dimensions with certain agglomeration. The conditions were suitable for the formation of the mesoporous structures when the PVP concentration was 50–75 mg mL^{-1}. Too low (25 mg mL^{-1}) and too high PVP concentration (150 mg mL^{-1}) led to the formation of nanocrystal clusters without distinct porous features by SEM. The dimension of the spherical nanostructures and the primary nanoparticles gradually decreased with an increasing concentration of PVP. The control experiment indicates that PVP with the appropriate concentration is critical for the formation of hierarchical nanostructures with mesoporous features.

Fig. 4 presents the typical morphology of the products under different hydrothermal treatment temperatures and their surface properties were presented in Table 1. It was found that with elevating the hydrothermal temperature, the products exhibit a typical spherical morphology but with an increase in the surface

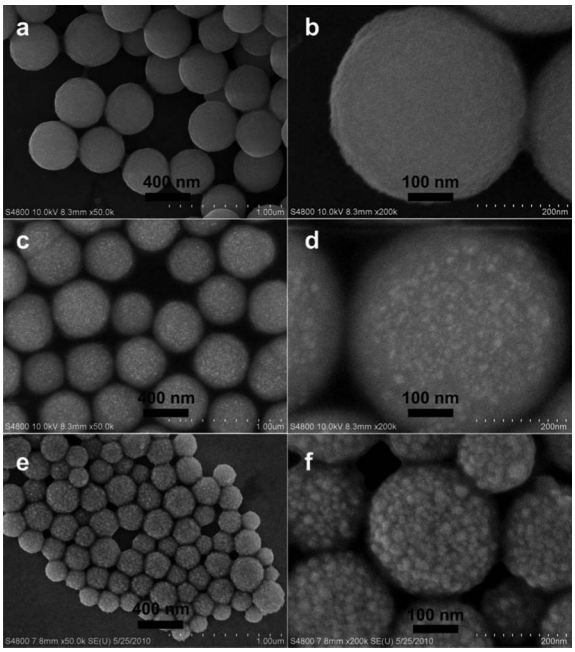

Fig. 4 SEM images of ZnS nanostructures obtained under different hydrothermal temperatures: (a) and (b) 100 °C, (c) and (d) 140 °C, and (e) and (f) 160 °C.

roughness; moreover, the primary nanoparticles as building blocks grew larger and the dimension of the nanospheres became slightly smaller. Accordingly, the higher hydrothermal treatment temperature led to the higher specific surface area and the larger pore volume. Similar phenomena were observed in the time-dependent experiment (ESI,† Fig. S4). The products transform from solid nanospheres (1 h) to nanocrystal clusters ($\geqslant$6 h), accompanied with the coarseness of primary nanoparticles and the slight shrinkage of the nanospheres. This evidence strongly supports the presumption that the primary nanoparticles firstly nucleated based on the coordination interaction between zinc ions and PVP with the addition of TAA. Further hydrothermal treatment led to the growth of ZnS nuclei in the Ostwald ripening process, which aggregated into a spherical morphology to minimize their surface energy; and the higher reaction temperature might accelerate this process, leaving behind the porous nanostructures. TGA analysis shows that ZnS MHNSs have a fraction of PVP with the weight percent accounting for *ca.* 8% of the total amount in the typical synthesis and, also, we can conclude that ZnS MHNSs were relatively stable below 350 °C (ESI,† Fig. S5).

3.3 Gas-sensing properties of ZnS MHNSs

The gas sensing properties of ZnO nanostructures have been widely investigated by many research groups.[37] However, the gas sensing performance of ZnS nanostructures has scarcely been investigated. Recently, ZnS nanobelts and nanowires were used to fabricate gas sensors with excellent sensing properties.[26,27] In this paper, we studied the gas sensing properties of ZnS MHNSs, and discussed the effect of morphology on the gas sensing responses. Here, six typical reducing gases (acetone, ethanol, gasoline, NH_3, HCHO, H_2S) and two typical oxidizing gases (SO_2 and Cl_2) were selected as target gases to investigate the gas response. As shown in Fig. 5, the gas sensor based on ZnS MHNSs shows better sensitivity and excellent selectivity to gasoline compared to the other tested gases.

Table 1 Surface properties of ZnS nanostructures prepared under different hydrothermal temperatures

Hydrothermal temperature (°C)	S_{BET} ($m^2\ g^{-1}$)	Pore volume ($cm^3\ g^{-1}$)	Crystallite size (nm)
100	8.1	0.032	—
140	17.8	0.039	10
160	24.1	0.056	16
180	58.4	0.292	30

The sensitivity of the sensors changed with the applied voltage, corresponding to the working temperature. We investigated the temperature-dependent behavior of the ZnS MHNSs-based sensors to 100 ppm gasoline and also compared the sensitivity of ZnS solid nanospheres obtained at 100 °C (Fig. 4a). As shown in Fig. 6, the response of the ZnS MHNSs-based sensor to gasoline increased with increasing working temperature in the range of 160 °C to 290 °C; with a further increase of the operating temperature up to 350 °C, the response decreased. The optimum working temperature of the ZnS MHNSs-based sensor to gasoline is determined to be 290 °C. Comparative analysis also clearly shows that the sensing response of ZnS MHNSs under each temperature point is much higher than that of the solid nanospheres. Considering the smaller specific surface area of the solid nanospheres, the enhancement of the gasoline sensing response of ZnS MHNSs could be attributed to more active sites derived from the porous structure. The higher surface accessibility provides more chances for the interaction between ZnS and the tested gases and thus higher sensitivity.[38–41]

The dynamic response of ZnS MHNSs-based sensors to 100 ppm gasoline is shown in Fig. 7, which provides more information for a sensing device: sensitivity, response time and recovery time. When the sensor was exposed to gasoline, the voltage promptly increased and rapidly reached a relatively stable value, and the response time is about 7 s. When the gasoline was switched off, the voltage abruptly decreased and then reached a relatively stable value, and the recovery time is less than 5 s. Therefore, it can be concluded that the ZnS MHNSs-based sensor exhibits attractive gasoline sensing behavior with excellent selectivity and fast response.

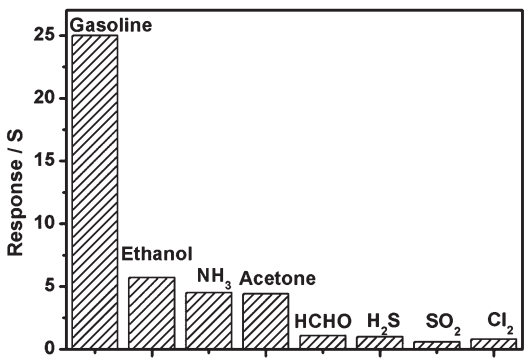

Fig. 5 Responses of the ZnS MHNSs-based sensor to various gases. The concentration of all the tested gases was 100 ppm and the operating temperature was 290 °C.

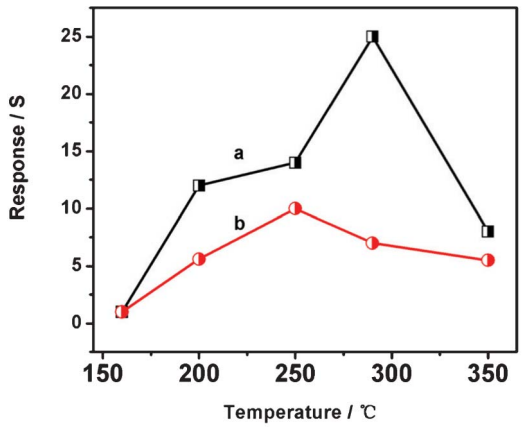

Fig. 6 Gas responses to 100 ppm gasoline as a function of operating temperature for ZnS with different morphologies: (a) mesoporous nanospheres and (b) solid nanospheres.

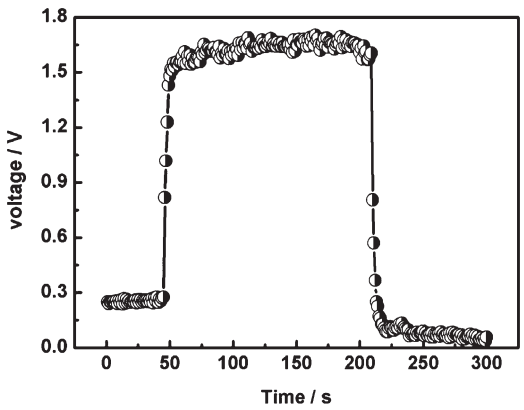

Fig. 7 Response transients of the ZnS MHNSs-based sensor to 100 ppm gasoline at 290 °C.

4 Conclusions

In summary, ZnS MHNSs were successfully prepared with $Zn(Ac)_2{\cdot}2H_2O$ and TAA as the raw materials in the presence of PVP aqueous solution *via* a low-cost, hydrothermal route. ZnS MHNSs exhibit a kind of hierarchical structure with mesoporous features, which consist of smaller building blocks assembled together. Also, a plausible mechanism based on coordination nucleation and subsequent Ostwald ripening is proposed. This helps us to have a good understanding of the process and experimental parameters that regulate the formation and direct the design and fabrication of other porous structures. By virtue of the interesting porous structure, a gasoline sensor based on ZnS MHNSs was achieved with excellent selectivity and fast response. Furthermore, ZnS MHNSs are also expected to be attractive for other surface-related applications such as photocatalysts because of the low cost of their large scale production, coupled with the tremendous advantages in easy separation, recovery, and recycling in industrial applications.

Acknowledgements

This work was financially supported by National Natural Science Foundation of China (21101056, 21105021) and Educational Commission of Henan Province of China (2011A150005).

References

1 J. Park, K. An, Y. Hwang, J. G. Park, H. J. Noh, J. Y. Kim, J. H. Park, N. M. Hwang and T. Hyeon, *Nat. Mater.*, 2004, **3**, 891.
2 S. H. Liu, R. M. Xing, F. Lu, R. K. Rana and J. J. Zhu, *J. Phys. Chem. C*, 2009, **113**, 21042.
3 Z. H. Jing and J. H. Zhan, *Adv. Mater.*, 2008, **20**, 4547.
4 Q. Peng, S. Xu, Z. B. Zhuang, X. Wang and Y. D. Li, *Small*, 2005, **1**, 216.
5 Y. Guo, J. Wang, Z. Tao, F. Dong, K. Wang, X. Ma, P. Yang, P. Hu, Y. Xu and L. Yang, *CrystEngComm*, 2012, **14**, 1185.
6 J. Liu, Y. C. Zhou, C. P. Liu, J. B. Wang, Y. Pan and D. F. Xue, *CrystEngComm*, 2012, **14**, 2669.
7 J. Liu, H. Xia, L. Lu and D. F. Xue, *J. Mater. Chem.*, 2010, **20**, 1506.
8 J. Liu, F. Liu, K. Gao, J. S. Wu and D. F. Xue, *J. Mater. Chem.*, 2009, **19**, 6073.
9 K. Y. Xue, D. R. Chen and X. L. Jiao, *Inorg. Chem.*, 2010, **49**, 1191.
10 Z. X. Sun, Q. Zhang, Y. H. Lu and Y. L. Li, *Microporous Mesoporous Mater.*, 2008, **109**, 376.
11 J. Liu and D. F. Xue, *Nanosci. Nanotechnol. Lett.*, 2011, **3**, 337.
12 J. Wu and D. F. Xue, *Nanosci. Nanotechnol. Lett.*, 2011, **3**, 371.
13 X. W. Lou, L. A. Archer and Z. Yang, *Adv. Mater.*, 2008, **20**, 3987.
14 J. S. Hu, L. S. Zhong, W. G. Song and L. J. Wan, *Adv. Mater.*, 2008, **20**, 2977.
15 S. Liu, H. Zhang and M. T. Swihart, *Nanotechnology*, 2009, **20**, 235603.
16 M. Hafeez, U. Manzoor and A. S. Bhatti, *J. Mater. Sci.: Mater. Electron.*, 2011, **22**, 1772.
17 R. M. Xing and S. H. Liu, *Nanoscale*, 2012, **4**, 3135.
18 S. M. Scholz, R. Vacassy, L. Lemaire, J. Dutta and H. Hofmann, *Appl. Organomet. Chem.*, 1998, **12**, 327.
19 Y. Yu, G. Chen, Q. Wang and Y. Li, *Energy Environ. Sci.*, 2011, **4**, 3652.
20 Q. Zhang, W. Chi, W. Zhang, C. Lv and J. Li, *New J. Chem.*, 2012, **36**, 119.
21 Y. Liu, J. Hu, C. Ngo, S. Prikhodko, S. Kodambaka, J. Li and R. Richards, *Appl. Catal., B*, 2011, **106**, 212.
22 J. Yang, J. J. Peng, R. X. Zou, F. Peng, H. J. Wang, H. Yu and J. Y. Lee, *Nanotechnology*, 2008, **19**, 7.
23 M. Muruganandham, R. Amutha and M. Sillanpaa, *ACS Appl. Mater. Interfaces*, 2008, **2**, 1817.
24 J. S. Hu, L. L. Ren, Y. G. Guo, H. P. Liang, A. M. Cao, L. J. Wan and C. L. Bai, *Angew. Chem., Int. Ed.*, 2005, **44**, 1269.
25 Y. H. Shi, J. Chen and P. W. Shen, *J. Alloys Compd.*, 2007, **441**, 337.
26 X. Wang, Z. Xie, H. Huang, Z. Liu, D. Chen and G. Shen, *J. Mater. Chem.*, 2012, **22**, 6845.
27 Z. G. Chen, J. Zou, G. Liu, H. F. Lu, F. Li, G. Q. Lu and H. M. Cheng, *Nanotechnology*, 2008, **19**, 5.
28 Z. Jiang, H. Sun, Z. Qin, X. Jiao and D. Chen, *Chem. Commun.*, 2012, **48**, 3620.
29 D. Son, A. Wolosiuk and P. V. Braun, *Chem. Mater.*, 2009, **21**, 628.
30 X. X. Yu, J. G. Yu, B. Cheng and B. B. Huang, *Chem.–Eur. J.*, 2009, **15**, 6731.
31 G. H. Yue, P. X. Yan, D. Yan, X. Y. Fan, M. X. Wang, D. M. Qu and J. Z. Liu, *Appl. Phys. A: Mater. Sci. Process.*, 2006, **84**, 409.
32 F. Piret, C. Bouvy and B. L. Su, *J. Mater. Chem.*, 2009, **19**, 5964.
33 H. Zhou, T. Fan, D. Zhang, Q. Guo and H. Ogawa, *Chem. Mater.*, 2007, **19**, 2144.
34 S. H. Liu, S. F. Tian and R. M. Xing, *CrystEngComm*, 2011, **13**, 7258.
35 S. H. Liu, F. Lu, X. D. Jia, F. F. Cheng, L. P. Jiang and J. J. Zhu, *CrystEngComm*, 2011, **13**, 2425.
36 C. J. Mao, X. W. Hu, J. M. Song, H. L. Niu and S. Y. Zhang, *CrystEngComm*, 2012, DOI: 10.1039/c2ce25853f.
37 J. Zhang, S. R. Wang, M. J. Xu, Y. Wang, B. L. Zhu, S. M. Zhang, W. P. Huang and S. H. Wu, *Cryst. Growth Des.*, 2009, **9**, 3532.
38 D. D. Vuong, G. Sakai, K. Shimanoe and N. Yamazoe, *Sens. Actuators, B*, 2005, **105**, 437.
39 N. Pinna, G. Neri, M. Antonietti and M. Niederberger, *Angew. Chem., Int. Ed.*, 2004, **43**, 4345.
40 M. E. Franke, T. J. Koplin and U. Simon, *Small*, 2006, **2**, 36.
41 W. Y. Li, L. N. Xu and J. Chen, *Adv. Funct. Mater.*, 2005, **15**, 851.